文章编号：1001-9014(2024)03-0421-14

DOI:10.11972/j.issn.1001-9014.2024.03.017

Pixel gradient-based adaptive iterative median filter for image impulse noise removal

JIN Xiang-Bo[1,2], WANG Yue-Ming[1,2*]

(1. Key Laboratory of Space Active Opto-Electronics Technology, Shanghai Institute of Technical Physics, Chinese Academy of Sciences, Shanghai 200083, China;
2. University of Chinese Academy of Sciences, Beijing 100049, China)

Abstract: Image impulse noise removal is essential for obtaining high-quality images. A novel pixel gradients-based adaptive iterative median filter is proposed to remove image impulse noise by utilizing the principles of thermal infrared camera imaging. Firstly, the maximum pixel gradient of the original image is computed based on the camera´s modulation transfer function (MTF), and a corresponding set of pixel gradients is established. Subsequently, the gradient weight root-mean-square error (GWRMSE) set of the original image and the corresponding pixel gradient filtered image is computed, and the optimal pixel gradient is determined as the one corresponding to the maximum value of Gaussian distribution of the GWRMSE set. Finally, the adaptive window size and number of iterations for the proposed filter are determined according to the density and complexity of the impulse noise in the image. Extensive experimental results demonstrate that the proposed filter exhibits excellent robustness in removing 8-bit and 16-bit single-channel impulse noise images. In comparison with other state-of-the-art methods, the proposed method can remove low-density random-valued impulse noise (RVIN) and salt-and-pepper noise (SAPN) in real thermal infrared camera-acquired images in real-time while preserving more than 99.5% of original pixels during the noise removal process. Additionally, for high-density SAPN removal, the proposed method achieves competitive results, demonstrating better peak signal-to-noise ratio (PSNR) and structural similarity index (SSIM) in comparison with filtering methods of faster running time and faster execution time in comparison with denoising methods of superior PSNR and SSIM. Moreover, it can recover meaningful image details even for images severely damaged by extreme SAPN (99%).

Key words: image denoising, adaptive iterative median filter, pixel gradient, Modulation Transfer Function, impulse noise

基于像素梯度自适应迭代中值滤波器的图像脉冲噪声抑制算法

金祥博[1,2], 王跃明[1,2*]

(1. 中国科学院上海技术物理研究所 空间主动光电技术重点实验室,上海 200083;
2. 中国科学院大学,北京 100049)

摘要:图像脉冲噪声移除是获得高质量图像的关键。本文通过热红外相机成像原理研究,提出了一种基于像素梯度自适应迭代中值滤波器的图像脉冲噪声抑制算法。首先,根据相机的调制传递函数计算获取原始图像的最大像素梯度,继而建立相应的像素梯度集合。然后,计算原始图像与对应像素梯度滤波图像的梯度权重均方根误差集合,并将该集合高斯分布的最大值对应的像素梯度确定为最佳像素梯度。最后,根据图像中脉冲噪声的密度和复杂度,确定所提滤波器的自适应窗口大小和迭代次数。大量实验结果表明,所提滤波器对移除8位、16位的单通道脉冲噪声图像展现出良好的鲁棒性。与其他先进方法相比,该方法可以实时移除真实热红外相机采集图像中低密度的随机值脉冲噪声和SAPN,并实现噪声抑制过程中99.5%以上的原始像素不会遭受破坏。除此之外,针对高密度SAPN抑制,该方法获得了具有竞争力的结果,与运行时间较快的滤

Received date: 2023-09-11, **Revised date**: 2024-02-25 **收稿日期**:2023-09-11,**修回日期**:2024-02-25

Foundation items: The study was by funded by the National Civil Aerospace Project of China (D040102)

Biography: JIN Xiang-Bo (1995-), male, Baiyin, China, Ph. D. Research interests involves remote sensing image processing, optical correction, geometric correction and 3D reconstruction. E-mail: jinxiangbo@mail.sitp.ac.cn.

* **Corresponding author**: E-mail: wangym@mail.sitp.ac.cn.

波方法相比表现出较好的PSNR和SSIM,与PSNR和SSIM较优秀的去噪方法相比表现出较快的运行时间。对于极限SAPN(99%)破坏的图像,也能够恢复有意义的图像细节。

关 键 词:图像去噪;自适应迭代中值滤波器;像素梯度;调制传递函数;脉冲噪声

中图分类号:TN215;TPT51.1 **文献标识码**:A

Introduction

Image impulse noise removal is a crucial preprocessing step for obtaining high-quality images in various digital image processing applications, including aerospace, biomedical engineering, industrial inspection, and robot vision. Impulse noise contamination can occur during acquisition, transmission, and recording due to different factors such as detector and circuit systems, channel transmission errors, non-ideal media between the scene and the imaging system, and memory location errors in the hardware components[1]. Impulse noise affects only some of the pixels of an image while leaving others unaffected. Two major impulse noise models, namely the salt-and-pepper noise (SAPN) model, where the noise pixels assume only the highest and lowest values of the digital number (DN) in the dynamic range of the image, and the random-valued impulse noise (RVIN) model, where the noise pixels can assume value in the dynamic range of the image with equal probability, have been described in the literature [2].

The median filter (MF) [3] has gained wide application due to its simple structure, fast execution time, and ability to preserve edge information. However, a limitation of the MF is its poor noise removal performance since it replaces the DN value of each pixel with the median found within a specific window. Therefore, various variants of the MF have been developed, such as the weighted median filter (WMF)[4], center-weighted median filter (CWMF) [5], adaptive median filter (AMF) [6], adaptive switching median filter (ASMF) [7-9], progressive switching median filter (PSMF) [10], adaptive dual-threshold median filter (ADTMF) [11], directional difference-based switching median filter (DD-SMF) [12], decision-based filters [13], spatially varying median filter (SVMF) [14], and three-state median filter (TSMF) [15]. These methods improve the MF′s ability to remove high-density impulse noise by detecting noisy pixels within the window. Furthermore, some enhanced versions, such as the effectively improved boundary discriminative noise detection filter (IBDNDF)[16], the switching adaptive median and fixed weighted mean filter[17], the unsymmetric trimmed adaptive median filter (UTAMF)[18], and the median-type noise detectors and the detail-preserving regularization method[19], also exhibit better performance and can successfully recover meaningful image details even from images damaged by 90% SAPN.

Of course, researchers have also contributed excellent image-denoising strategies from other theoretical aspects. Chen *et al.* [20] proposed a weighted coupled sparse representation model with classified regularization to remove impulse noise in images by dividing image pixels into clear, slightly damaged, and severely damaged pixels. The low-rank Hankel matrix based on the annihilating filter is a compelling image restoration method. Jin *el at.* [21] extended this idea and proposed a sparse and low-rank decomposition of a Hankel-structured matrix for impulse noise removal. In Ref. [22], the authors presented an adaptive detail-preserving filter based on a cloud model that can remove up to 95% of SAPN while preserving good image details. Fuzzy theory is often used to solve uncertainty problems and has profound implications for image denoising. For example, the adaptive network-based fuzzy inference system filter and the regression-based neuro-fuzzy network trained by the ABC algorithm can eliminate impulse noise [23-24]. Besides, Ahmed *el at.* [1] proposed an iterative adaptive fuzzy filter using alpha-trimmed mean that can retrieve meaningful details even at up to 97% SAPN. Singh *el at.* [25] achieved excellent results on standard test images with 20% to 99% SAPN damage using their proposed adaptive type-2 fuzzy filter.

In recent years, deep learning has been widely applied to image denoising, particularly for Gaussian noise, Gaussian additive white noise, and Gaussian-impulse mixture noise [26-30]. However, only a few deep-learning models have been used for impulse noise removal. Notable examples include the denoising framework based on deep convolutional neural network (CNN) for suppressing impulse noise in color images [31], the efficient CNN with particle swarm optimization (PSO) model for high-density impulse noise removal [32], the CNN-based image restoration method for impulse noise removal [33], and the switching filtering technique using deep learning for impulse noise removal [34]. They accomplish image denoising through two main processes: 1) utilizing neural networks to detect impulse noise in the image and 2) inputting the detection results into the denoising module to reconstruct the denoised image.

Although various variants of median filters, fuzzy filters, and image denoising and restoration models based on deep learning have been developed by previous researchers, only some have explored image noise removal strategies from the fundamental level of digital camera imaging principles. Digital cameras are complex products that integrate optics, mechanical structures, and electronics. During imaging, the image sensor (CCD or CMOS) converts light signals into discrete electronic signals, which are further converted into digital signals. The number of pixels on the image sensor is represented as a matrix of rows and columns, where the numerical signal in each cell corresponds to the DN value in the digital image. Due to design errors in optical devices, the resolution of the image sensor, the wave-particle duality of light, and the complexity of the observed area, neighboring pixels exhibit subtle differences, which can be understood as pixel gradients between adjacent pixels.

Therefore, by exploring the camera imaging model, we propose an adaptive iterative median filter based on pixel gradients, summarized as follows.

1) The modulation transfer function (MTF), as a performance indicator of the camera, can calculate the maximum pixel gradient of the captured image and establish a pixel gradient set. Subsequently, the gradient weight root-mean-square error (GWRMSE) set of the original image and the corresponding pixel gradient filtered image is computed. The Gaussian distribution of the GWRMSE set is calculated using a Gaussian function. Finally, the pixel gradient corresponding to the Gaussian distribution′s maximum value is considered the optimal pixel gradient for removing the impulse noise in the image.

2) Our proposed filter consists of two types of median filters. The first type includes two orthogonal judgment-based median filters with window sizes 3×3, combined with the optimal pixel gradient for real-time removal of the image′s discrete, low-density RVIN and SAPN. The second type is an adaptive window size median filter combined with the optimal pixel gradient and SAPN attribute set for removing high-density SAPN.

3) The adaptive window size and number of iterations are determined based on the density and complexity of the impulse noise in the image, and the proposed filter is used to achieve noise removal.

1 Methods

Digital images are represented using a two-dimensional array, where the rows and columns determine the position of each pixel in the image. The DN value of a pixel represents the grayscale value with statistical spatial characteristics. During the imaging process, the camera discretizes the shape of objects into points, lines, and surfaces. Uniformly distributed objects in the scene should have the same DN value for all pixels in the image. However, due to limitations imposed by the camera′s optical system and image sensor materials and design techniques, each pixel only represents the statistical properties of the corresponding region. In other words, the DN values of pixels representing the same object can vary, as shown in Fig. 1. Therefore, we propose using pixel gradients to describe the fluctuation range in non-uniform DN values.

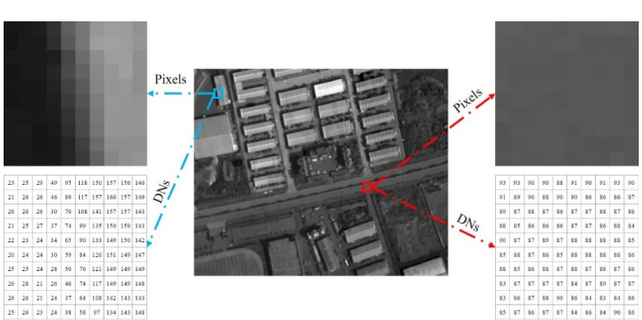

Fig. 1　Distribution of pixel DN values in a uniform region and an edge region on the image
图1　图像上均匀区域和边缘区域分布的像素DN值

1.1 Modulation transfer function (MTF)

The MTF[35] provides an intuitive description of the transfer process of light information through optical media and devices. It comprehensively and objectively characterizes the sharpness of images. The corresponding formula is as follows:

$$\mathrm{MTF}(\omega_x,\omega_y)=\left|H(\omega_x,\omega_y)\right|=\frac{I(\omega_x,\omega_y)}{O(\omega_x,\omega_y)}\quad,\quad(1)$$

where $I(\omega_x,\omega_y)$ and $O(\omega_x,\omega_y)$ are the spatial spectrum of the image and object, respectively. $H(\omega_x,\omega_y)$ is the Fourier transform of the point spread function, called the optical transfer function. ω_x and ω_y are 2D spatial frequencies expressed in terms of circular frequencies.

The light distribution of an optical image can be regarded as a combination of countless spatial frequency sinusoidal wave distributions. Specific frequency sinusoidal grating stripes define the modulation depth of the sinusoidal distribution, and testing requires projection brightness with a sinusoidal variation as the target. However, this poses a significant challenge for production. To facilitate laboratory MTF testing, a square wave target corresponding to the limiting spatial frequencies is commonly used[36], as shown in Fig. 2(a).

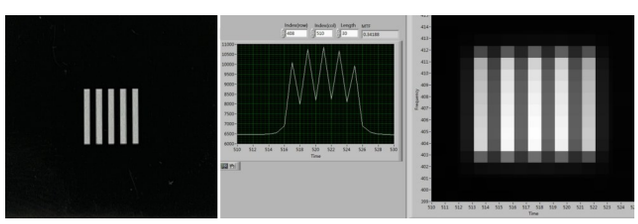

Fig. 2　(a) The square wave target; (b) MTF calibration of mid-wave infrared camera using a square wave target
图2　(a)方波靶标;(b)使用方波靶标进行中波红外相机MTF测试

When a mid-wave infrared imaging system captures an image of a square wave target, the system outputs the peak intensity $I_{\max}$ corresponding to the transparent slits and the valley intensity $I_{\min}$ corresponding to the target surface patterns, as shown in Fig. 2(b). In this way, the contrast transfer function (CTF) can be represented as the ratio between the amplitude of signal fluctuations and the average signal level, as follows:

$$\mathrm{CTF}=\frac{I_{\max}-I_{\min}}{I_{\max}+I_{\min}}\quad,\quad(2)$$

Since the square wave signal can be expanded into a Fourier series of its fundamental frequency and its multiples of AC signals, the CTF can also be expressed as the sum of the MTF of the fundamental frequency and its multiples of the square wave signal as the following:

$$\mathrm{CTF}=\frac{4}{\pi}\left[\mathrm{MTF}-\frac{\mathrm{MTF}}{3}+\frac{\mathrm{MTF}}{5}-\frac{\mathrm{MTF}}{7}+\cdots\right],\quad(3)$$

When the frequency of the square wave signal exceeds 1/3 the cut-off frequency, the higher order terms MTF can be ignored. CTF is redefined as:

$$\mathrm{CTF}=\frac{4}{\pi}\mathrm{MTF}\quad,\quad(4)$$

1.2 Optimal pixel gradient

Once the optical calibration of the imaging system is completed in the laboratory, the optimal MTF value of the camera is determined. This allows for the calculation of the maximum gradient $g_{\max}$ between adjacent pixels, as mentioned below:

$$g_{\max} = I_{\max} - I_{\min} = \frac{4}{\pi}(I_{\max} + I_{\min}) \times \mathrm{MTF} \quad , \quad (5)$$

In practical scenarios, due to losses during light propagation, the relative brightness values of the highlights in the image are lower than those of the scene. Conversely, due to the effects of stray light, scattering, and diffraction, the relative brightness values of the shadows in the image are higher than those of the scene. However, for an ideal optical system without aberrations, stray light, scattering, reflection, or absorption, the described situation would not occur. Nonetheless, they all satisfy the following equation:

$$(I_{\max} + I_{\min}) \equiv I_{\max}^{\mathrm{dr}} - I_{\min}^{\mathrm{dr}} \quad , \quad (6)$$

where $I_{\max}^{\mathrm{dr}}$ denotes the maximum value of the dynamic range of the image acquired by the camera in the corresponding spectral range. Similarly, $I_{\min}^{\mathrm{dr}}$ represents the minimum value of the dynamic range of the image captured by the camera in the corresponding spectral range.

By utilizing the optimal MTF value of the camera, we can calculate the maximum gradient $g_{\max}$ between adjacent pixels. This allows for the representation of the pixel gradient set of the camera's captured image $\boldsymbol{G}$, as mentioned below:

$$\boldsymbol{G} = \left\{ g_k \middle| 1 \leqslant g_k \leqslant g_{\max}, g_k \in N \right\} \quad , \quad (7)$$

where g_k is the k-th pixel gradient of the set $\boldsymbol{G}$.

In addition to the factors influencing the brightness values of the image mentioned earlier, the optical system is also affected by the presence of objects and background in the imaging area. Each pixel captures the DN value corresponding to the imaged area. Specifically, when the pixel's imaged area corresponds to an object's surface, the DN value represents the light information from the object, and the optical system solely influences the gradient between adjacent pixels. However, when the pixel's imaged area falls on the edge of an object, the DN value represents both the light information from the object and the background. The optical system and the background brightness values influence the gradient between adjacent pixels. Therefore, it is necessary to determine an optimal pixel gradient for a specific optical imaging system.

Firstly, based on the proposed filter, we calculated the root-mean-square error r_k between the pixel gradient g_k corresponding to the filtered image $\boldsymbol{I}_k$ and the original image $\boldsymbol{I}_o$, as shown below:

$$r_k(\boldsymbol{I}_k) = \sqrt{\frac{\sum_{i=1}^{M}\sum_{j=1}^{N}(\boldsymbol{I}_o(i,j) - \boldsymbol{I}_k(i,j))^2}{M \times N}} \quad , \quad (8)$$

where $M \times N$ is the image size.

To ensure a more precise assessment of the optimal pixel gradient based on the computed $r_k(\boldsymbol{I}_k)$ for different pixel gradients g_k, we have conducted further calculations of $r_k(\boldsymbol{I}_k)$ within a unit pixel gradient, as follows:

$$h_k(r_k, g_k) = \frac{r_k(\boldsymbol{I}_k)}{g_k} \quad , \quad (9)$$

where $h_k(r_k, g_k)$ denotes the GWRMSE of $r_k(\mathbf{I}_k)$ with respect to the pixel gradient g_k.

In this manner, we can represent the pixel gradients set $\boldsymbol{G}$ corresponding to the GWRMSE set $\boldsymbol{H}$ as follows:

$$\boldsymbol{H} = \left\{ ((r_k, g_k), h_k(r_k, g_k)), \forall r_k \Leftrightarrow g_k \in \boldsymbol{G} \right\} \quad , \quad (10)$$

Subsequently, we have employed a Gaussian function to establish a Gaussian distribution model $\boldsymbol{A}$ for the GWRMSE set $\boldsymbol{H}$, which can be expressed as:

$$f_k(h_k) = \mathrm{e}^{-\frac{h_k - \mu}{2\sigma^2}} \quad , \quad (11)$$

$$\mu = \frac{\sum_{k=1}^{n} h_k}{n} \quad , \quad (12)$$

$$\sigma = \sqrt{\frac{\sum_{k=1}^{n}(h_k - \mu)}{n}} \quad , \quad (13)$$

$$\boldsymbol{A} = \left\{ (h_k, f_k(h_k)), \forall h_k \in \boldsymbol{H} \right\} \quad , \quad (14)$$

where f_k is the Gaussian function corresponding to the GWRMSE h_k. μ denotes the mean value of the set $\boldsymbol{H}$. σ denotes the standard deviation of the set $\boldsymbol{H}$. n denotes the full number of elements of the set $\boldsymbol{H}$.

Finally, we designate the maximum element in set $\boldsymbol{A}$ to correspond to the h_k element in set $\boldsymbol{H}$, which in turn corresponds to the g_k element in the set $\boldsymbol{G}$, as the optimal pixel gradient g_{opt} for image filtering, as follows:

$$g_{\mathrm{opt}} = \left\{ g_k \middle| \max(\boldsymbol{A}) \Leftrightarrow h_k \Leftrightarrow g_k, \forall h_k \in \boldsymbol{H}, \forall g_k \in \boldsymbol{G} \right\}, \quad (15)$$

1.3 Theory of the proposed filter

Based on the calculated optimal pixel gradient, we can determine the optimal fluctuation range among neighboring pixels in the original image, including the surface and edge of the feature. In other words, when the pixel gradient between the central pixel and its neighboring pixels is less than the optimal pixel gradient, we consider the central pixel to be not impulse noise; otherwise, it is classified as impulse noise.

The proposed filter utilizes two types of MFs. The first type is primarily employed for real-time removal of dispersed, low-density RVIN and SAPN, employing two orthogonal-based MFs, F_1 and F_2, with window sizes of 3×3, as depicted in Fig. 3. F_1 considers the pixels above, below, left, and right of the center pixel as neighbors to form the orthogonal setup. Similarly, F_2 uses the pixels in the top-left, bottom-left, top-right, and bottom-right positions as neighbors to establish the orthogonal configuration. By establishing these two orthogonal relationships, we can determine if the center pixel satisfies the range defined by the optimal pixel gradient, allowing for rapid identification of whether the center pixel corresponds to impulse noise.

The decision formula for the center pixel, neighboring pixels, and optimal pixel gradient associated with F_1 is expressed as follows:

$$\begin{cases} \Delta g_{11}^{1} = p_{ij} - p_{i-1,j} - g_{\mathrm{opt}} \\ \Delta g_{12}^{1} = p_{ij} - p_{i+1,j} - g_{\mathrm{opt}} \\ \Delta g_{13}^{1} = p_{ij} - p_{ij-1} - g_{\mathrm{opt}} \\ \Delta g_{14}^{1} = p_{ij} - p_{ij+1} - g_{\mathrm{opt}} \end{cases} \quad , \quad (16)$$

$$\begin{cases} \Delta g_{21}^{1} = p_{i-1,j} - p_{i,j} - g_{\text{opt}} \\ \Delta g_{22}^{1} = p_{i+1,j} - p_{i,j} - g_{\text{opt}} \\ \Delta g_{23}^{1} = p_{i,j-1} - p_{i,j} - g_{\text{opt}} \\ \Delta g_{24}^{1} = p_{i,j+1} - p_{i,j} - g_{\text{opt}} \end{cases}, \quad (17)$$

where Δg_{11}^{1}, Δg_{12}^{1}, Δg_{13}^{1}, Δg_{14}^{1}, Δg_{21}^{1}, Δg_{22}^{1}, Δg_{23}^{1}, and Δg_{24}^{1} are the differences between the gradient of the central pixel $p_{i,j}$ and the adjacent pixels $p_{i-1,j}$, $p_{i+1,j}$, $p_{i,j-1}$ or $p_{i,j+1}$ minus the optimal pixel gradient g_{opt}.

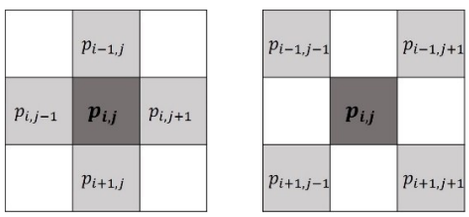

(a)　(b)

Fig. 3　(a) Orthogonal-based MF F_1; (b) (a) Orthogonal-based MF F_2

图3　(a)基于正交的中值滤波器F_1;(b)基于正交的中值滤波器F_2

The decision formula for the center pixel, neighboring pixels, and optimal pixel gradient associated with F_2 is expressed as follows:

$$\begin{cases} \Delta g_{11}^{2} = p_{i,j} - p_{i-1,j-1} - g_{\text{opt}} \\ \Delta g_{12}^{2} = p_{i,j} - p_{i+1,j-1} - g_{\text{opt}} \\ \Delta g_{13}^{2} = p_{i,j} - p_{i-1,j+1} - g_{\text{opt}} \\ \Delta g_{14}^{2} = p_{i,j} - p_{i+1,j-1} - g_{\text{opt}} \end{cases}, \quad (18)$$

$$\begin{cases} \Delta g_{21}^{2} = p_{i-1,j-1} - p_{i,j} - g_{\text{opt}} \\ \Delta g_{22}^{2} = p_{i+1,j-1} - p_{i,j} - g_{\text{opt}} \\ \Delta g_{23}^{2} = p_{i-1,j+1} - p_{i,j} - g_{\text{opt}} \\ \Delta g_{24}^{2} = p_{i+1,j-1} - p_{i,j} - g_{\text{opt}} \end{cases}, \quad (19)$$

where Δg_{11}^{2}, Δg_{12}^{2}, Δg_{13}^{2}, Δg_{14}^{2}, Δg_{21}^{2}, Δg_{22}^{2}, Δg_{23}^{2}, and Δg_{24}^{2} are the differences between the gradient of the central pixel $p_{i,j}$ and the adjacent pixels $p_{i-1,j-1}$, $p_{i+1,j-1}$, $p_{i+1,j-1}$ or $p_{i+1,j+1}$ minus the optimal pixel gradient g_{opt}.

When $\Delta g_{11}^{1} \geqslant 0$, $\Delta g_{12}^{1} \geqslant 0$, $\Delta g_{13}^{1} \geqslant 0$, and $\Delta g_{14}^{1} \geqslant 0$, or $\Delta g_{21}^{1} \geqslant 0$, $\Delta g_{22}^{1} \geqslant 0$, $\Delta g_{23}^{1} \geqslant 0$, and $\Delta g_{24}^{1} \geqslant 0$, or $\Delta g_{11}^{2} \geqslant 0$, $\Delta g_{12}^{2} \geqslant 0$, $\Delta g_{13}^{2} \geqslant 0$, and $\Delta g_{14}^{2} \geqslant 0$, or $\Delta g_{21}^{2} \geqslant 0$, $\Delta g_{22}^{2} \geqslant 0$, $\Delta g_{23}^{2} \geqslant 0$, and $\Delta g_{24}^{2} \geqslant 0$, the central pixel$p_{i,j}$ is classified as impulse noise. Subsequently, we need to establish a 3×3 window centered at $p_{i,j}$, where all the pixels within the window are utilized to restore the central pixel $p_{i,j}$ quickly. The corresponding set of pixel intensities $\boldsymbol{W}_{i,j}$, as follows:

$$\boldsymbol{W}_{ij} = \left\{ p_{i+kj+l} \middle| -1 \leqslant k,l \leqslant 1, k,l \in Z \right\}, \quad (20)$$

Finally, we use the median value $v_{i,j}$ of the set $\boldsymbol{W}_{i,j}$ instead of the center noise pixel $p_{i,j}$, as follows:

$$v_{ij} = \text{median}(W_{ij}) \quad (21)$$

where *median* denotes the median model for computing the set $\boldsymbol{W}_{i,j}$.

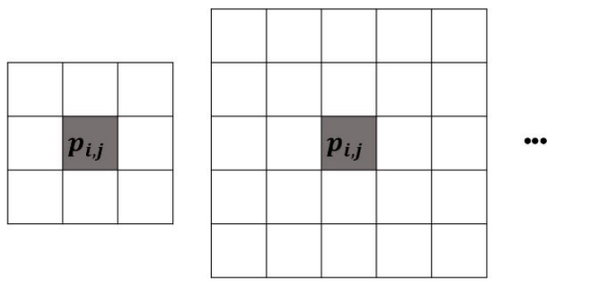

Fig. 4　MF F_3 with an adaptive window size, left window size T = 1, next window size T = 2

图4　基于自适应窗口大小的 MF F_3,第一个窗口大小T=1, 下一个窗口大小T=2

The second type of MF is primarily designed to remove high-density SAPN. It is an adaptive median filter F_3, which employs a variable window size, as illustrated in Fig. 4. The adaptive window size of F_3 is established around the central pixel $p_{i,j}$ as a $(2T+1)\times(2T+1)$ neighborhood, where the selection of the window size T depends on the SAPN density. The set of pixel intensities within the window is represented as $\boldsymbol{W}_{i,j}^{T}$, and it is expressed as follows:

$$\boldsymbol{W}_{ij}^{T} = \left\{ p_{i+k,j+l} \middle| -T \leqslant k,l \leqslant T, k,l,T \in N \right\}, \quad (22)$$

Then, the median value $v_{i,j}^{T}$ of $\boldsymbol{W}_{i,j}^{T}$ can be computed, and the SAPN within $\boldsymbol{W}_{i,j}^{T}$ can be effectively removed to form a new set $\boldsymbol{W}_{ne}^{T}$, as described in the following:

$$v_{ij}^{T} = \text{median}(\boldsymbol{W}_{ij}^{T}), \quad (23)$$

$$\boldsymbol{W}_{ne}^{T} = \complement_{\boldsymbol{W}_{ij}^{T}} \boldsymbol{S} \cap \complement_{\boldsymbol{W}_{ij}^{T}} \boldsymbol{P}, \quad (24)$$

where S denotes the salt noise set $\boldsymbol{S} = \left\{ I_{\max}^{\text{dr}}, I_{\max}^{\text{dr}} \in N \right\}$. $\boldsymbol{P}$ denotes the pepper noise set $\boldsymbol{P} = \left\{ I_{\min}^{\text{dr}}, I_{\min}^{\text{dr}} \in N \right\}$.

Subsequently, we can establish a weight set $\boldsymbol{C}$ to determine whether the center pixel $p_{i,j}$ is a noisy pixel based on the median value $v_{i,j}^{T}$ and the optimal pixel gradient g_{opt}, as shown below:

$$\boldsymbol{C} = \left\{ c \middle| v_{ij}^{T} - g_{\text{opt}} < c < v_{ij}^{T} + g_{\text{opt}}, c \in R \right\}, \quad (25)$$

where c denotes the element in the weight set $\boldsymbol{C}$. When $v_{i,j}^{T} - g_{\text{opt}} < I_{\min}^{\text{dr}}$, $v_{i,j}^{T} - g_{\text{opt}} = I_{\min}^{\text{dr}}$. When $v_{i,j}^{T} + g_{\text{opt}} > I_{\max}^{\text{dr}}$, $v_{i,j}^{T} + g_{\text{opt}} = I_{\max}^{\text{dr}}$.

Finally, we decide whether the center pixel $p_{i,j}$ is a noisy pixel. If $p_{i,j} \in \boldsymbol{C}$ or $\boldsymbol{W}_{ne}^{T} = \varnothing$, then $p_{i,j}$ is considered non-noisy. Otherwise, $p_{i,j}$ is a noisy pixel. We utilize the median value v_{ne}^{T} from the set $\boldsymbol{W}_{ne}^{T}$ to restore$p_{i,j}$, as illustrated below:

$$v_{ne}^{T} = \text{median}(\mathbf{W}_{ne}^{T}), \quad (25)$$

By proposing the pixel gradient-based adaptive median filter, we can effectively remove dispersed, low-density RVIN and SAPN in remote sensing images in real time and eliminate high-density SAPN in the image. The entire noise removal process is outlined in Algorithm 1. In general, for impulse noise images captured by the same camera, the pixel gradients for noise removal remain consistent due to the fixed MTF. When applying Algorithm 1 for the first time on an impulse noise image,

the proposed filter does not damage the regions unaffected by impulse noise interference. Similarly, successfully removed areas of impulse noise are not compromised during the iterative filtering process until all noise within the image is eliminated. It is important to emphasize that the number of iterations (Iters) and the adaptive window size (T) of Algorithm 1 are determined by the SAPN density (D), as indicated in Table 1.

Algorithm 1 Pixel gradient-based adaptive iterative MF

算法 1 基于像素梯度的自适应迭代中值滤波器

Input: Impulse noise image $\boldsymbol{I}_o$, optimal pixel gradient g_{opt}, adaptive window size T, impulse noise density D.

Output: Filtered image $\boldsymbol{I}_b$.

For all pixels $p_{i,j}$ in $\boldsymbol{I}_o$ **do**
  Calculate Δg_{11}^1, Δg_{12}^1, Δg_{13}^1, Δg_{14}^1, according to Ep. (16).
  If $\Delta g_{11}^1 \geqslant 0$ **and** $\Delta g_{12}^1 \geqslant 0$ **and** $\Delta g_{13}^1 \geqslant 0$**and** $\Delta g_{14}^1 \geqslant 0$
    Calculate $v_{i,j}$ according to Eps. (20) - (21). $p_{i,j}^b = v_{i,j}$.
  Calculate Δg_{21}^1, Δg_{22}^1, Δg_{23}^1, Δg_{24}^1, according to Ep. (17).
  Elseif $\Delta g_{21}^1 \geqslant 0$ **and** $\Delta g_{22}^1 \geqslant 0$ **and** $\Delta g_{23}^1 \geqslant 0$ **and** $\Delta g_{24}^1 \geqslant 0$
    Calculate $v_{i,j}$ according to Eps. (20) - (21). $p_{i,j}^b = v_{i,j}$.
  Calculate Δg_{11}^2, Δg_{12}^2, Δg_{13}^2, Δg_{14}^2, according to Ep. (18).
  Elseif $\Delta g_{11}^2 \geqslant 0$ **and** $\Delta g_{12}^2 \geqslant 0$ **and** $\Delta g_{13}^2 \geqslant 0$ **and** $\Delta g_{14}^2 \geqslant 0$
    Calculate $v_{i,j}$ according to Eps. (20) - (21). $p_{i,j}^b = v_{i,j}$.
  Calculate Δg_{21}^2, Δg_{22}^2, Δg_{23}^2, Δg_{24}^2, according to Ep. (19).
  Elseif $\Delta g_{21}^2 \geqslant 0$ **and** $\Delta g_{22}^2 \geqslant 0$ **and** $\Delta g_{23}^2 \geqslant 0$ **and** $\Delta g_{24}^2 \geqslant 0$
    Calculate $v_{i,j}$ according to Eps. (20) - (21). $p_{i,j}^b = v_{i,j}$.
  Else
    If $D \leqslant 1\%$
    $p_{i,j}^b = p_{i,j}$
    Else
    Calculate $\boldsymbol{W}_{i,j}^T$, $v_{i,j}^T$, $\boldsymbol{W}_{ne}^T$, $\boldsymbol{C}$, v_{ne}^T according to Eps. (22)-(26).
      If $p_{i,j} \in \boldsymbol{C}$
        $p_{i,j}^b = p_{i,j}$
      Elseif $\boldsymbol{W}_{ne}^T = \varnothing$
        $p_{i,j}^b = v_{i,j}^T$
      Else
        $p_{i,j}^b = v_{ne}^T$.
      End if
    End if
  End if
End for
All pixels $p_{i,j}^b$ in $\boldsymbol{I}_b$.

2 Results and Discussions

In this section, we use mid-wave infrared (MWIR) images, long-wave infrared (LWIR) images captured by real cameras, and open-access available datasets to validate the effectiveness of the proposed filters and compare them with state-of-the-art impulse noise filters. All experiments are conducted on an Intel Core i7-10700F 2.9 GHz processor with 16 GB RAM and NVIDIA GeForce GTX 1 660 Ti, running MATLAB 2019a.

Table 1 The division intervals of the SAPN density (D), and the corresponding number of iterations (I_{ters}) and adaptive window size (T)

表 1 椒盐噪声密度(D)的划分区间,以及对应的迭代次数(Iters)和自适应窗口大小(T)

D(%)	[0, 1]	(1, 20]	(20, 60]	(60, 80]	(80, 99]
I_{ters}	0	0	1	2	2
T	1	1	1/1	1/1/1	2~15/2/1

2.1 Optimal pixel gradients of camera

To validate the optimal pixel gradient g_{opt} computation model, we utilized 100 640×512, 16-bit MWIR raw images and 100 320×256, 16-bit LWIR raw images acquired by a thermal infrared array scanning camera, and the noise distribution models corresponding to the partial MWIR and LWIR raw images are shown in Fig. 5. The optical system of the thermal infrared array scanning camera is shown in Fig. 6, with corresponding parameters listed in Table 2. After laboratory optical calibration of the MWIR camera, the average MTF was measured to be 0.281 0 (the mean MTF value for the eight directions and centers of the image sensor). We are considering the maximum dynamic range of the MWIR camera as $I_{\max}^{\text{dr}} = 11\,000$ and the minimum dynamic range as $I_{\min}^{\text{dr}} = 8\,000$; the maximum pixel gradient achievable by this camera is $g_{\max} = 1\,073$. Consequently, the pixel gradient set $\boldsymbol{G} = \{1 \leqslant g_k \leqslant 1\,073\}$is established. Subsequently, utilizing the proposed method, we compute the GWRMSE set $\boldsymbol{H}$ and the corresponding Gaussian distribution set $\boldsymbol{A}$. By analyzing the distribution curves of the GWRMSE function $h_k(r_k, g_k)$ and the Gaussian function $f_k(h_k)$ with respect to the pixel gradient g_k, we determined that the optimal pixel gradient g_{opt} for a single MWIR raw image is 142, as depicted in Fig. 7.

Upon obtaining the optimal pixel gradient for impulse noise removal in the raw images, we applied our proposed filter to remove low-density impulse noise from 100 raw images. The impulse noise density $D \in [0, 1]$, the adaptive window size $T = 0$, and the partial filtering results are illustrated in Fig. 9. Through comparison, and it is evident that the proposed pixel gradient-based filter effectively eliminates impulse noise while preserving and restoring the fine details of the raw images. To provide a quantitative assessment, we conducted statistical analysis on the inconsistent pixels between the original and denoised images. For the 100 test images, the maximum proportion of inconsistent pixels was 0.396 7%, the minimum proportion was 0.221 1%, and the average proportion was 0.244 9%, as shown in Fig. 8(b). This indicates that the proposed filter preserves over 99.5% of the pixels without compromising their integrity during impulse noise removal. The denoised image corresponding to the maximum proportion is depicted in Fig. 9(b), exhibiting complex high-intensity features such as buildings with significant variations among adjacent pixels. The denoised image corresponding to the minimum pro-

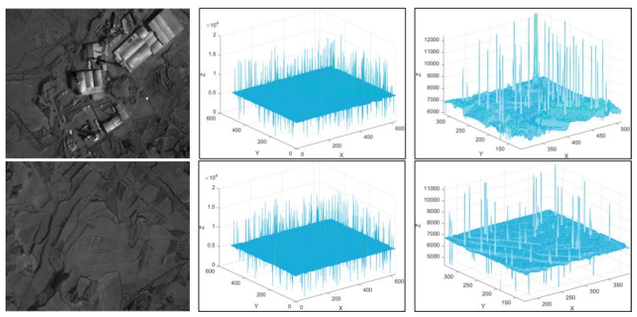

(a)

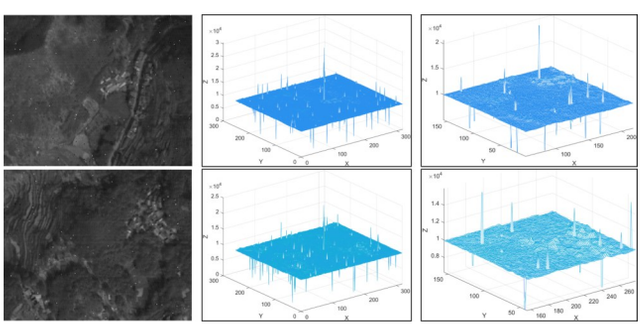

(b)

Fig. 5　(a) Impulse noise distribution of selected test images from 100 MWIR raw images; (b) Impulse noise distribution of selected test images from 100 LWIR raw images. The first column is the original images. The second column is the original image's pixel values distribution models. The third column is the second column's localized pixel value distribution models

图 5　(a) 100 幅中波红外原始图像中选取的测试图像的脉冲噪声分布;(b) 100 幅长波红外原始图像中选取的测试图像的脉冲噪声分布。第一列为原始图像。第二列是原始图像的像素值分布模型。第三列是第二列的局部像素值分布模型

Table 2　Main parameters of the thermal infrared array scanning camera

表 2　热红外面阵扫瞄相机的主要参数

Parameters	MWIR	LWIR
Spectral range	3~5 μm	8~12 μm
Array size	640×512	320×256
Focal length	120 mm	
Clear aperture	52 mm	
Pixel pitch	15 μm	30 μm
Field of view (FOV)	4.58°×3.67°	
Instantaneous FOV	125 μrad	250 μrad

portion is illustrated in Fig. 9(d), characterized by homogeneous low-intensity features like farmlands and mountains with minimal fluctuation between neighboring pixels. Throughout the entire noise removal process, the average computation time for all the images was 0.008 0 s, with a maximum of 0.017 0 s and a minimum of 0s, as displayed in Fig. 8(c). Therefore, our proposed filter enables real-time impulse noise removal in MWIR images, yielding excellent denoising results.

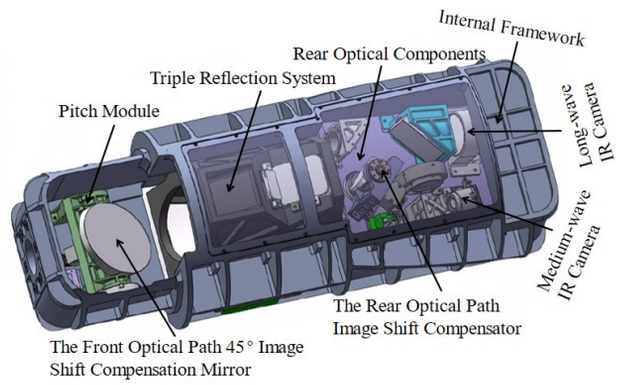

Fig. 6　The internal framework of the thermal infrared array scanning camera

图 6　热红外面阵扫瞄相机的内框架

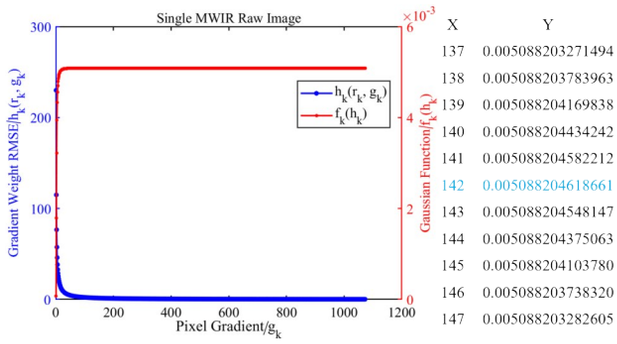

	X	Y
137		0.005088203271494
138		0.005088203783963
139		0.005088204169838
140		0.005088204434242
141		0.005088204582212
142		0.005088204618661
143		0.005088204548147
144		0.005088204375063
145		0.005088204103780
146		0.005088203738320
147		0.005088203282605

Fig. 7　Distribution curves of pixel gradient g_k corresponding to gradient weight RMSE $h_k(r_k, g_k)$ and Gaussian function $f_k(h_k)$ for a single MWIR raw image, and the computed optimal pixel gradient g_{opt}

图 7　单张中波红外原始图像的像素梯度 g_k 对应的梯度权重 RMSE $h_k(r_k, g_k)$ 和高斯函数 $f_k(h_k)$, 以及计算的最佳像素梯度 gopt

Similarly, after laboratory optical calibration of the LWIR camera, the average MTF was measured to be 0.270 4. Considering the maximum dynamic range of the LWIR camera as $I_{\max}^{\mathrm{dr}} = 12\,000$ and the minimum dynamic range as $I_{\min}^{\mathrm{dr}} = 9\,000$, the maximum pixel gradient achievable by this camera is $g_{\max} = 1\,033$. Consequently, the pixel gradient set $\boldsymbol{G} = \{1 \leqslant g_k \leqslant 1\,033\}$ is established for the LWIR camera. Therefore, the optimal pixel gradient for the 100 LWIR raw images is 137, as illustrated in Fig. 10(a).

The impulse noise density $D \in [0, 1]$ of the LWIR raw images, so the adaptive window size of the proposed filter to be $T = 0$. Through quantitative analysis and visual inspection of the denoised images from the 100 LWIR raw images, the maximum proportion of inconsistent pixels was found to be 0.319 4%, the minimum proportion was 0.215 4%, and the average proportion was 0.228 4%, as shown in Fig. 10(b). This indicates that over 99.5% of the LWIR image pixels remain intact, largely preserving the original pixel while effectively removing the impulse noise in the images, as illustrated in Fig. 11. Specifically, because there is a stripe noise[37] in Fig. 11

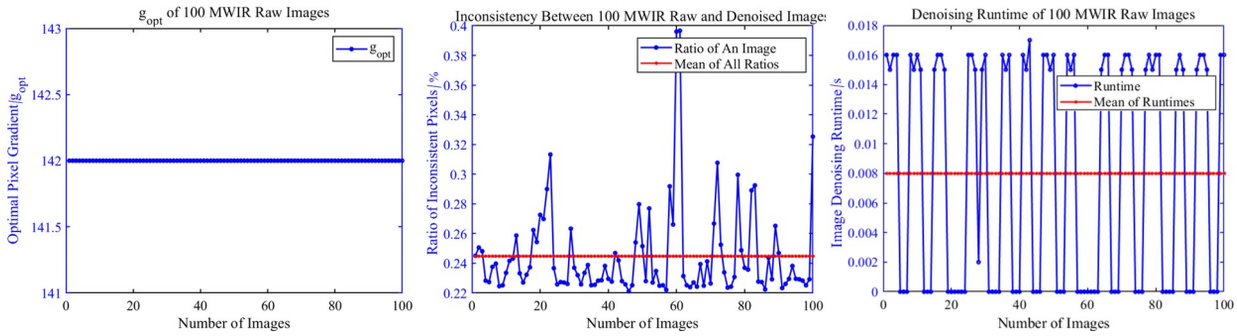

Fig. 8 （a）Optimal pixel gradient g_{opt} of 100 MWIR raw images；（b）running time of 100 MWIR raw images with noise removed；（c）Inconsistent pixels ratio（%）of the 100 MWIR raw images corresponding to the denoised image

图 8 （a）100 张中波红外原始图像的最优像素梯度 g_{opt}；（b）100 张中波红外图像移除噪声时的运行时间；（c）100 张中波红外原始图像对应去噪图像的不一致像素比例（%）

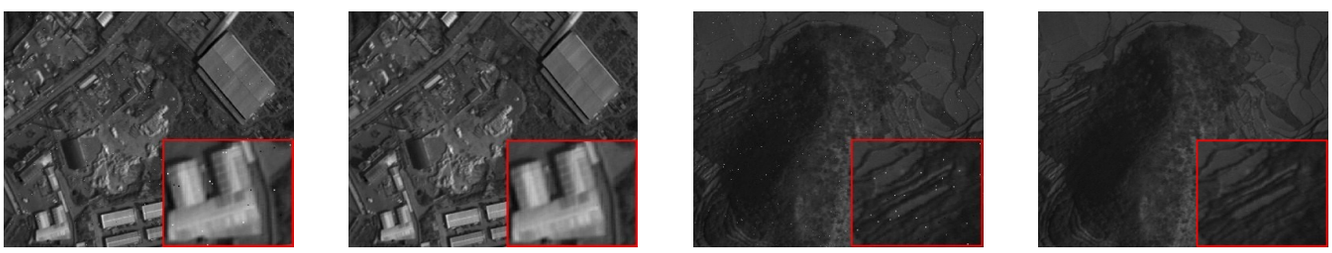

（a） （b） （c） （d）

Fig. 9 (a) and (c) are the MWIR raw images；(b) and (d) are correspondingly noise-removed images.

图 9 （a）和（c）是中波红外原始图像；（b）和（d）是对应的噪声移除图像

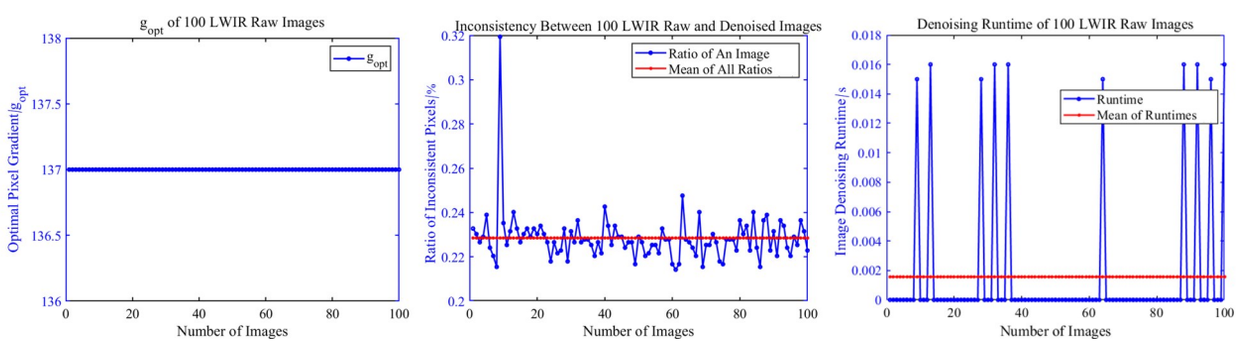

Fig. 10 （a）Optimal pixel gradient g_{opt} of 100 LWIR raw images；（b）running time of 100 LWIR raw images with noise removed；（c）Inconsistent pixels ratio（%）of the 100 LWIR raw images corresponding to the denoised image

图 10 （a）100 张长波红外原始图像的最优像素梯度 g_{opt}；（b）100 张长波红外图像移除噪声时的运行时间；（c）100 张长波红外原始图像对应去噪图像的不一致像素比例（%）

（a） （b） （c） （d）

Fig. 11 (a) and (c) are the LWIR raw images；(b) and (d) are correspondingly noise-removed images

图 11 （a）和（c）是长波红外原始图像；（b）和（d）是对应的噪声移除图像

Table 3　Comparison of the mean ratio (%) of inconsistent pixels for 100 MWIR raw images and the corresponding denoised images by different state-of-the-art methods.
表3　不同先进方法对100张中波热红外图像和对应去噪图像的不一致像素的平均比例(%)。

Images	Methods							
	MF	BdCNN	HONTV-OGS	ℓ_0-OGSTV	DTN	DCNN	ALOHA	Proposed
MWIR	67. 643 4	84. 524 8	82. 050 9	78. 674 2	61. 525 5	7. 231 9	4. 392 1	0. 244 9
LWIR	73. 323 6	86. 445 5	83. 694 3	80. 691 6	63. 758 6	8. 844 4	3. 073 6	0. 228 4

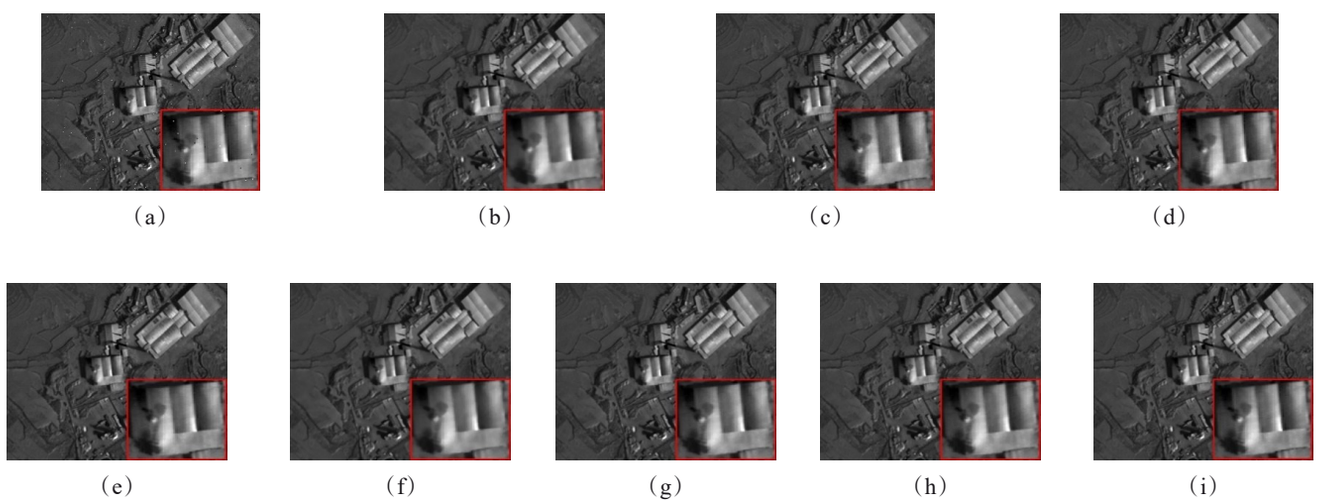

Fig. 12　Different state-of-the-art methods for denoising MWIR raw images: (a) raw image; (b) MF; (c) BdCNN; (d) HONTV-OGS; (e) ℓ_0-OGSTV; (f) DTN; (g) DCNN; (h) ALOHA; (i) Proposed
图12　不同先进方法对中波红外原始图像去噪:(a)原始图像;(b)MF;(c)BdCNN;(d)HONTV-OGS;(e)ℓ_0-OGSTV;(f)DTN;(g)DCNN;(h)ALOHA;(i)Proposed

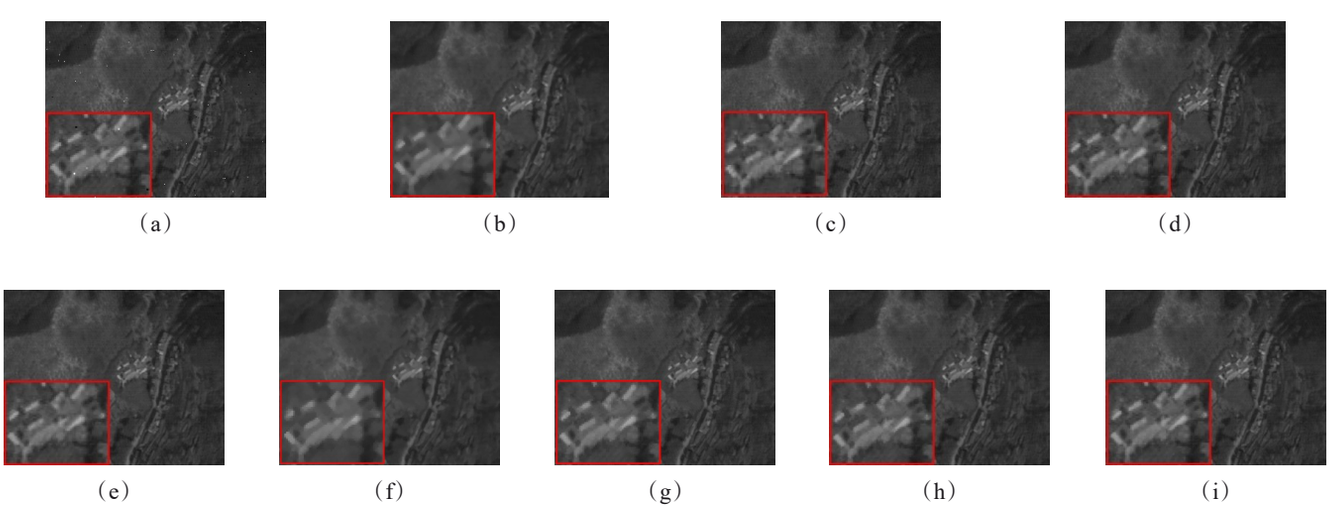

Fig. 13　Different state-of-the-art methods for denoising LWIR raw images: (a) raw image; (b) MF; (c) BdCNN; (d) HONTV-OGS; (e) ℓ_0-OGSTV; (f) DTN; (g) DCNN; (h) ALOHA; (i) Proposed
图13　不同先进方法对长波红外原始图像去噪:(a)原始图像;(b)MF;(c)BdCNN;(d)HONTV-OGS;(e)ℓ0-OGSTV;(f)DTN;(g)DCNN;(h)ALOHA;(i)Proposed

(a), Fig. 11(b) represents the denoised image corresponding to the maximum proportion. At the same time, Fig. 11(d) depicts the denoised image corresponding to the minimum proportion. Throughout the entire noise removal process, the average computation time for all the images was 0. 001 6 s, with a maximum of 0. 016 0 s and a minimum of 0s, as displayed in Fig. 10(c). Therefore, the proposed optimal pixel gradient model and filter demonstrate real-time impulse noise removal in LWIR camera-captured images.

2.2 Comparison with other state-of-the-art methods through MWIR and LWIR images

In this section, we compare the proposed method with seven filtering methods, including Median Filter (MF)[3], blind denoising convolutional neural network (BdCNN)[38], high-order nonconvex total variation and overlapping group sparsity (HONTV-OGS) fusion method[39], ℓ_0 overlapping group sparse total variation (ℓ_0-OGSTV) method[40], distribution transformation network (DTN)[41], deep convolutional neural network (DCNN)[33], and rank-deficient hankel matrix-based low-rank approximation (ALOHA) method[21], using the MWIR and LWIR raw images. The denoised results of the MWIR and LWIR raw images are presented in Figs. 12 and 13, respectively. It is evident that all seven advanced filtering methods and our proposed method effectively remove discrete and low-density RVIN from the images while restoring rich image details. Additionally, we computed the average proportion of inconsistent pixels before and after denoising for 100 MWIR and 100 LWIR original images, as shown in Table 3. It is clear that our proposed pixel gradient-based method successfully removes RVIN in the original images while preserving over 99.5% of the original pixels. In contrast, the other methods have caused varying degrees of damage to the original pixels in the images.

2.3 Comparison of high-density SAPN with state-of-the-art methods

This section compares the proposed filter with seven advanced impulse noise filtering methods through simulation experiments to evaluate its denoising performance on high-density SAPN. The quality of the denoised images is quantitatively evaluated using the peak signal-to-noise ratio (PSNR) and structural similarity index (SSIM). PSNR measures the noise density relative to the original image[42]. SSIM, which approximates human visual perception, assesses the similarity between the processed and original images[42]. Generally, higher values of PSNR and SSIM indicate that the quality of the processed image approaches that of the original image. The definitions of PSNR and SSIM are as follows:

$$\mathrm{PSNR} = 10 \times \log_{10}\left(\frac{(I_{\max}^{\mathrm{dr}} - I_{\min}^{\mathrm{dr}})^2}{\mathrm{MSE}}\right), \quad (27)$$

where MSE is the mean square error of the original image I_o and the processed image I_p.

$$\mathrm{SSIM} = \frac{(2\mu_{I_o}\mu_{I_p} + C_1)(2\sigma_{I_oI_p} + C_2)}{(\mu_{I_o}^2 + \mu_{I_p}^2 + C_1)(\sigma_{I_o}^2 + \sigma_{I_p}^2 + C_2)}, \quad (28)$$

where μ_{I_o}, μ_{I_p}, σ_{I_o}, σ_{I_p}, and $\sigma_{I_oI_p}$ are the local means, standard deviations, and cross-covariance for images $I_o$and I_p, respectively. $C_1$and $C_2$are two constants, $C_1 = \left[0.01(I_{\max}^{\mathrm{dr}} - I_{\min}^{\mathrm{dr}})\right]^2$, $C_2 = \left[0.03(I_{\max}^{\mathrm{dr}} - I_{\min}^{\mathrm{dr}})\right]^2$.

Firstly, we selected six different types of 512×512, 8-bit publicly available grayscale test images for SAPN simulation, as shown in Fig. 14. Since the camera's MTF of the simulated images is unknown, use SPAN to destroy the standard test images. Then, according to the characteristics of SAPN, the optimal pixel gradient $g_{\mathrm{opt}} = 255$ for all test images and the salt noise set $\boldsymbol{S} = \{255\}$ and pepper noise set $\boldsymbol{P} = \{0\}$. Finally, the proposed method and seven comparative denoising methods are applied to the standard test images for SAPN removal, and the quality of the resulting images is quantitatively evaluated using PSNR and SSIM. Meanwhile, the computational efficiency of all denoising methods is assessed based on their running time under the same conditions.

Figs. 15, 16, and 17 present the restoration results of the test images after being contaminated with SAPN for both the comparative and proposed methods. For the 20% SAPN corrupted test image, all the methods can effectively remove the impulse noise from the image and maintain good image details, except for the MF method restored image, which suffers from severe smoothing. For the test images damaged by 50% SAPN, the MF and BdCNN methods recovery results suffer

from severe smoothing. For the test images damaged by 80% SAPN, the restoration results of the MF, BdCNN, and HONTV-OGS methods exhibit severe distortion. In contrast, the other methods produce excellent denoising results, maintaining the integrity of the image content, including our proposed method. However, our method exhibits poor recovery results compared to the other four methods. Although the object's structure in the image is intact, the gradient of the pixels at the object's edges falls off so much that the replacement pixels are easily affected by the neighboring pixels and do not reach the gray value of the original pixels. Moreover, our proposed method can effectively restore meaningful image details even for images severely damaged by extreme SAPN. As demonstrated in Fig. 18, although the image's texture suffers severe damage and smoothing, the edges of the objects in the image are well restored and preserved, and the visual analysis can still distinguish different features.

Fig. 14 Test images: (a) Lena; (b) Bridge; (c) Pepper; (d) Baboon; (e) Boat; (f) Barbara
图14 测试图像:(a)莉娜;(b)桥;(c)辣椒;(d)狒狒;(e)船;(f)芭芭拉

Table 4　Compared the proposed method with seven state-of-the-art filtering methods by PSNR (dB) and SSIM for $D = \{20\%,50\%,80\%\}$SAPN

表 4　针对 $D=\{20\%,50\%,80\%\}$SAPN，提出的方法通过 PSNR 和 SSIM 与七种先进的滤波方法进行比较

Method	PSNR (dB)						SSIM					
	Image											
	(a)	(b)	(c)	(d)	(e)	(f)	(a)	(b)	(c)	(d)	(e)	(f)
D = 20%												
NOISY	12.43	12.24	12.31	12.54	12.45	12.38	0.083 2	0.177 3	0.083 9	0.215 4	0.113 9	0.138 7
MF	31.18	24.68	31.38	22.33	27.92	24.21	0.909 7	0.717 7	0.909 3	0.640 3	0.831 9	0.747 0
BdCNN	38.43	30.55	33.79	29.47	35.29	33.49	0.965 8	0.927 8	0.938 3	0.931 5	0.945 2	0.956 9
HONTV-OGS	39.25	32.16	38.99	29.76	37.41	32.41	0.961 4	0.945 1	0.954 0	0.934 9	0.954 3	0.938 8
ℓ_0-OGSTV	40.72	33.53	40.53	31.08	38.91	33.69	0.972 5	0.958 6	0.967 8	0.948 9	0.966 4	0.950 4
DTN	42.63	32.48	40.16	29.62	38.49	34.07	0.988 6	0.961 2	0.980 2	0.952 3	0.975 4	0.969 4
DCNN	43.13	33.02	42.10	30.68	39.56	40.13	0.984 0	0.946 8	0.980 2	0.968 8	0.972 1	0.982 1
ALOHA	45.23	32.43	43.61	31.44	42.70	44.95	0.994 2	0.961 7	0.990 1	0.965 4	0.990 9	0.993 8
Proposed	39.58	31.63	38.55	28.95	35.58	30.59	0.984 7	0.951 1	0.981 8	0.938 3	0.968 0	0.955 9
D = 50%												
NOISY	8.46	8.26	8.31	8.57	8.49	8.43	0.025 0	0.0549	0.026 3	0.069 0	0.349	0.044 8
MF	24.89	21.17	25.09	19.75	23.03	22.03	0.807 3	0.5171	0.832 5	0.432 8	0.682 6	0.637 1
BdCNN	32.71	25.51	32.03	23.32	29.50	27.70	0.914 8	0.7551	0.899 4	0.710 9	0.860 6	0.840 4
HONTV-OGS	34.33	27.30	35.17	24.70	32.44	26.57	0.920 6	0.8201	0.913 4	0.775 5	0.886 2	0.801 2
ℓ_0-OGSTV	38.91	29.98	38.60	26.85	35.89	28.42	0.967 6	0.9130	0.959 7	0.882 4	0.949 6	0.896 3
DTN	36.36	27.70	37.93	24.95	32.72	27.67	0.954 6	0.8751	0.963 6	0.843 5	0.921 5	0.887 7
DCNN	36.55	28.38	35.35	26.44	34.20	33.18	0.950 0	0.8978	0.946 4	0.880 2	0.923 1	0.958 7
ALOHA	38.61	27.64	37.63	26.10	35.32	38.94	0.975 8	0.8781	0.962 4	0.876 6	0.958 1	0.978 0
Proposed	33.58	26.45	32.38	24.03	29.86	25.75	0.946 2	0.8422	0.938 5	0.804 7	0.897 1	0.859 2
D = 80%												
NOISY	6.43	6.21	6.27	6.53	6.44	6.37	0.009 3	0.016 9	0.009 6	0.021 0	0.012 3	0.013 8
MF	18.75	17.20	18.07	16.72	17.67	18.53	0.661 9	0.309 5	0.687 2	0.268 5	0.501 8	0.515 1
BdCNN	22.52	19.84	22.14	18.41	20.86	20.98	0.661 2	0.414 1	0.679 8	0.339 3	0.567 1	0.549 2
HONTV-OGS	26.98	18.64	21.83	20.20	21.33	22.41	0.726 0	0.350 0	0.632 1	0.338 2	0.507 4	0.550 8
ℓ_0-OGSTV	31.96	24.90	31.56	22.41	28.63	24.88	0.921 7	0.753 5	0.914 5	0.674 7	0.860 8	0.770 7
DTN	30.18	23.70	29.46	21.26	27.18	23.59	0.870 3	0.674 7	0.866 0	0.600 3	0.796 2	0.716 9
DCNN	32.46	24.58	31.29	22.31	29.14	26.28	0.918 7	0.750 4	0.886 7	0.652 1	0.846 2	0.832 9
ALOHA	32.44	23.89	32.26	22.08	28.82	31.57	0.921 6	0.687 3	0.904 8	0.651 6	0.851 4	0.924 0
Proposed	28.68	22.58	27.78	20.56	25.60	22.61	0.864 0	0.646 7	0.851 6	0.553 8	0.762 9	0.707 8

Table 4 presents the PSNR and SSIM of all test images after being corrupted by SAPN and restored using all filtering methods. Correspondingly, Table 5 provides the average running time of all filtering methods for denoising all test images. Through comprehensive analysis, our proposed method demonstrates excellent denoising results compared to the MF, BdCNN, and HONTV-OGS methods.

Compared to the ℓ_0-OGSTV, DTN, DCNN, and ALOHA methods, although our proposed method does not exhibit superior image restoration, it requires less denoising time. In summary, our proposed denoising method performs well, showing excellent PSNR and SSIM compared to some faster methods. In terms of methods

Table 5　Compared the proposed method with seven state-of-the-art filtering methods by running time (s) for $D = \{20\%,50\%,80\%\}$SAPN

表 5　针对 $D=\{20\%,50\%,80\%\}$SAPN，提出的方法通过运行时间(s)与七种先进的滤波方法进行比较

D (%)	Methods							
	MF	BdCNN	HONTV-OGS	ℓ_0-OGSTV	DTN	DCNN	ALOHA	Proposed
20%	0.001 1	0.563 3	34.121 7	12.379 1	6.376 4	7.842 1	4 721.424 2	0.622 7
50%	0.001 1	0.564 6	34.442 1	14.974 5	6.404 9	7.839 6	3 328.851 1	1.303 9
80%	0.001 1	0.560 3	36.056 9	19.057 6	6.405 5	7.830 4	1 780.774 5	1.944 0

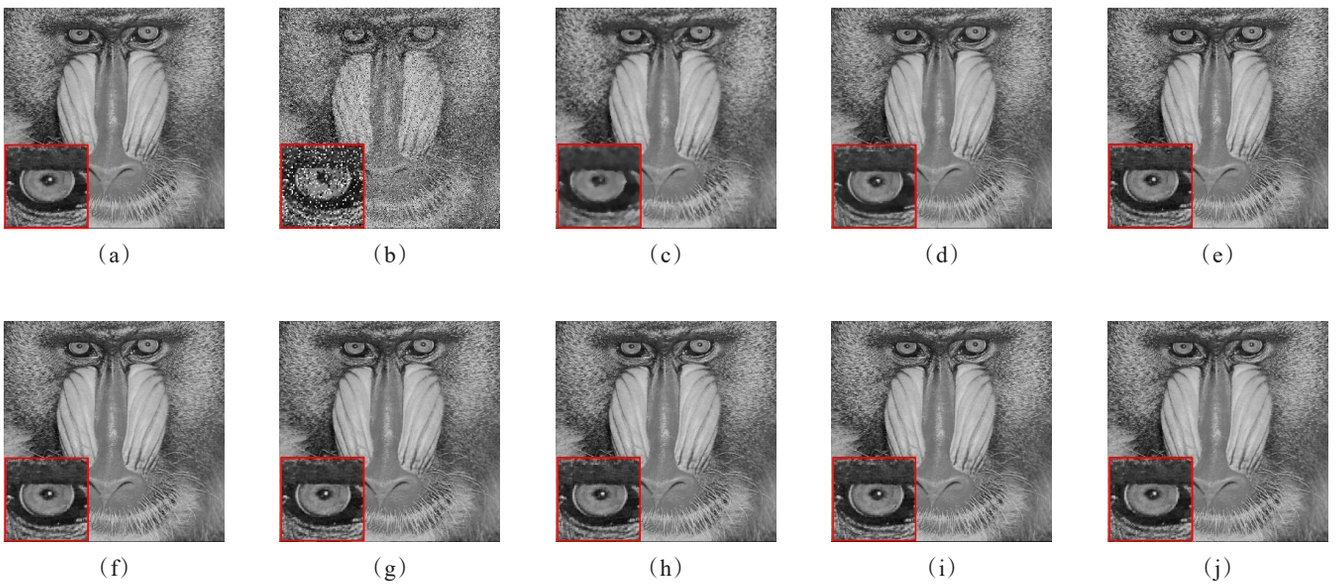

Fig. 15 Denoised results of Baboon test images: (a) Clean image; (b) noisy image with 20% SAPN; (c) MF; (d) BdCNN; (e) HONTV-OGS; (f) ℓ_0-OGSTV; (g) DTN; (h) DCNN; (i) ALOHA; (j) Proposed
图15 Baboon测试图像的去噪结果:(a)干净图像;(b)20%SAPN的噪声图像;(c)MF;(d)BdCNN;(e)HONTV-OGS;(f)ℓ_0-OGSTV;(g)DTN;(h)DCNN;(i)ALOHA;(j)Proposed

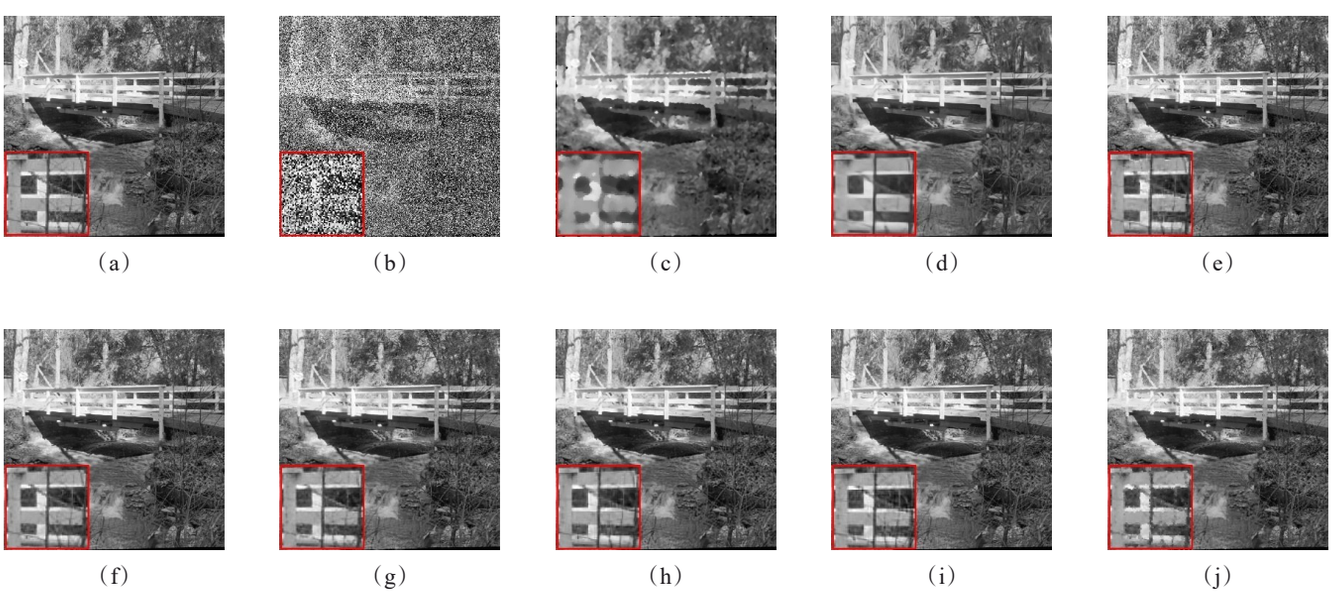

Fig. 16 Denoised results of Bridge test images: (a) Clean image; (b) noisy image with 50% SAPN; (c) MF; (d) BdCNN; (e) HONTV-OGS; (f) ℓ_0-OGSTV; (g) DTN; (h) DCNN; (i) ALOHA; (j) Proposed
图16 Bridge测试图像的去噪结果:(a)干净图像;(b)50%SAPN的噪声图像;(c)MF;(d)BdCNN;(e)HONTV-OGS;(f)ℓ_0-OGSTV;(g)DTN;(h)DCNN;(i)ALOHA;(j)Proposed

with superior PSNR and SSIM performance, our proposed method demonstrates a speedier computation time. Besides, our proposed method can remove SAPN from 0% to 99%.

3 Conclusion

This paper proposes a pixel gradients-based adaptive iterative median filter to remove low-density impulse noise and 0% to 99% SAPN in single-channel images. Firstly, based on the imaging principle of optical cameras, we utilize the camera's MTF to obtain the maximum pixel gradient of the original image and establish the pixel gradients set of that camera. Next, we calculate the GWRMSE between the original image and the corresponding pixel gradient filtered image. Finally, the optimal pixel gradient is determined as the one correspond-

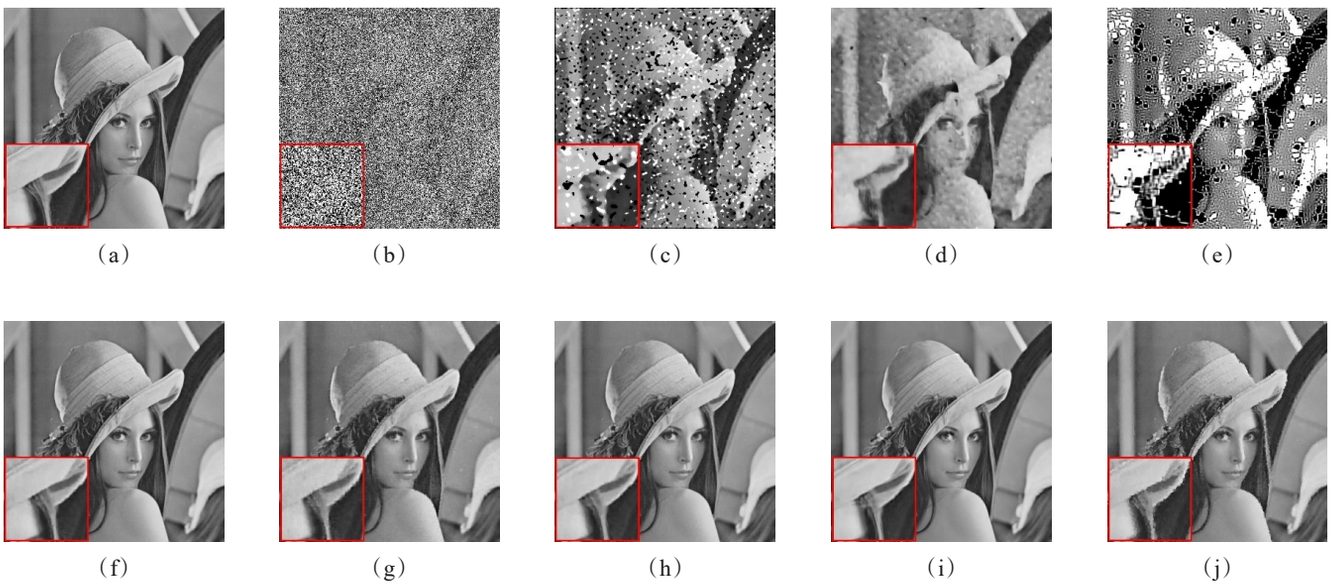

Fig. 17　Denoised results of Lena test images: (a) Clean image; (b) noisy image with 80% SAPN; (c) MF; (d) BdCNN; (e) HONTV-OGS; (f) ℓ_0-OGSTV; (g) DTN; (h) DCNN; (i) ALOHA; (j) Proposed
图 17　Lena 测试图像的去噪结果:(a)干净图像;(b)80%SAPN 的噪声图像;(c)MF;(d)BdCNN;(e)HONTV-OGS;(f)ℓ_0-OGSTV;(g)DTN;(h)DCNN;(i)ALOHA;(j)Proposed

Fig. 18　Denoising results of Boat test images at extreme SAPN: (a) clean image; (b) noisy image with 97% SAPN; (c) recovered image of the proposed method; (d) noisy image with 99% SAPN; (e) recovered image of the proposed method
图 18　极限 SAPN 下的 Boat 测试图像的去噪结果:(a)干净图像;(b)97%SAPN 的噪声图像;(c)所提方法的恢复图像;(d)99%SAPN 的噪声图像;(e)所提方法的恢复图像

ing to the maximum value of the Gaussian distribution of the GWRMSE set. By considering the noise density and complexity of the impulse noise, we can determine the adaptive window size of the proposed filter and the required number of iterations to remove the impulse noise in the image. Extensive experimental results demonstrate that the developed filter exhibits robustness in removing 8-bit and 16-bit single-channel impulse noise images, effectively removing low-density RVIN from real thermal infrared camera-acquired images in real-time. Compared to other advanced methods, this approach achieves a preservation rate of 99.5% of the original pixels during denoising. Furthermore, for high-density SAPN in images, our proposed filter obtains competitive results compared to advanced filtering methods, showing better PSNR and SSIM compared to faster filtering methods and faster computation time compared to methods with superior PSNR and SSIM. Additionally, for images severely damaged by extreme SAPN, the proposed method can recover meaningful image details.

References

[1] Ahmed F, Das S. Removal of high-density salt-and-pepper noise in images with an iterative adaptive fuzzy filter using alpha-trimmed mean [J]. *IEEE Transactions on Fuzzy Systems*. 2013, **22**(5): 1352-1358.
[2] Petrovic N I, Crnojevic V. Universal impulse noise filter based on genetic programming [J]. *IEEE Transactions on Image Processing*. 2008, **17**(7): 1109-1120.
[3] Nodes T, Gallagher N. Median filters: Some modifications and their properties [J]. *IEEE Transactions on Acoustics, Speech, and Signal Processing*. 1982, **30**(5): 739-746.
[4] Brownrigg DR. The weighted median filter [J]. *Communications of the ACM*. 1984, **27**(8): 807-818.
[5] Ko S J, Lee Y H. Center weighted median filters and their applications to image enhancement [J]. *IEEE Transactions on Circuits and Systems*. 1991, **38**(9): 984-993.
[6] Hwang H, Haddad R A. Adaptive median filters: New algorithms and results [J]. *IEEE Transactions on Image Processing*. 1995, **4**(4): 499-502.

[7] Fabijańska A, Sankowski D. Noise adaptive switching median-based filter for impulse noise removal from extremely corrupted images [J]. *IET Image Processing*. 2011, **5**(5):472-480.
[8] Akkoul S, Ledee R, Leconge R, *et al*. A new adaptive switching median filter [J]. *IEEE Signal Processing Letters*. 2010, **17**(6): 587-590.
[9] Eng H L, Ma K K. Noise adaptive soft-switching median filter [J]. *IEEE Transactions on Image Processing*. 2001, **10**(2):242-251.
[10] Wang Z, Zhang D. Progressive switching median filter for the removal of impulse noise from highly corrupted images [J]. *IEEE Transactions on Circuits and Systems II: Analog and Digital Signal Processing*. 1999, **46**(1):78-80.
[11] Gupta V, Chaurasia V, Shandilya M. Random-valued impulse noise removal using adaptive dual threshold median filter [J]. *Journal of Visual Communication and Image Representation*. 2015, **26**:296-304.
[12] Hashimoto Y, Kajikawa Y, Nomura Y. Directional difference-based switching median filters [J]. *Electronics and Communications in Japan (Part III: Fundamental Electronic Science)*. 2002, **85**(3): 22-32.
[13] Srinivasan K S, Ebenezer D. A new fast and efficient decision-based algorithm for removal of high-density impulse noises [J]. *IEEE Signal Processing Letters*. 2007, **14**(3):189-192.
[14] Chen T, Wu H R. Space variant median filters for the restoration of impulse noise corrupted images [J]. *IEEE Transactions on Circuits and Systems II: Analog and Digital Signal Processing*. 2001, **48**(8): 784-789.
[15] Chen T, Ma K K, Chen L H. Tri-state median filter for image denoising [J]. *IEEE Transactions on Image Processing*. 1999, **8**(12): 1834-1838.
[16] Jafar I F, AlNa'mneh R A, Darabkh K A. Efficient improvements on the BDND filtering algorithm for the removal of high-density impulse noise [J]. *IEEE Transactions on Image Processing*. 2012, **22**(3): 1223-1232.
[17] Mafi M, Rajaei H, Cabrerizo M, *et al*. A robust edge detection approach in the presence of high impulse noise intensity through switching adaptive median and fixed weighted mean filtering [J]. *IEEE Transactions on Image Processing*. 2018, **27**(11):5475-5490.
[18] Esakkirajan S, Veerakumar T, Subramanyam AN, *et al*. Removal of high-density salt and pepper noise through modified decision based unsymmetric trimmed median filter [J]. *IEEE Signal Processing Letters*. 2011, **18**(5):287-290.
[19] Chan R H, Ho C W, Nikolova M. Salt-and-pepper noise removal by median-type noise detectors and detail-preserving regularization [J]. *IEEE Transactions on Image Processing*. 2005, **14**(10): 1479-1485.
[20] Chen C L, Liu L, Chen L, et al. Weighted couple sparse representation with classified regularization for impulse noise removal [J]. *IEEE Transactions on Image Processing*. 2015, **24**(11):4014-4026.
[21] Jin K H, Ye J C. Sparse and low-rank decomposition of a Hankel structured matrix for impulse noise removal [J]. *IEEE Transactions on Image Processing*. 2017, **27**(3):1448-1461.
[22] Zhou Z. Cognition and removal of impulse noise with uncertainty [J]. *IEEE Transactions on Image Processing*. 2012, **21**(7):3157-3167.
[23] Civicioglu P. Using uncorrupted neighborhoods of the pixels for impulsive noise suppression with ANFIS [J]. *IEEE Transactions on Image Processing*. 2007, **16**(3):759-773.
[24] Caliskan A, Cil Z A, Badem H, *et al*. Regression-based neuro-fuzzy network trained by ABC algorithm for high-density impulse noise elimination [J]. *IEEE Transactions on Fuzzy Systems*. 2020, **28**(6):1084-1095.
[25] Singh V, Dev R, Dhar N K, *et al*. Adaptive type-2 fuzzy approach for filtering salt and pepper noise in grayscale images [J]. *IEEE Transactions on Fuzzy Systems*. 2018, **26**(5):3170-3176.
[26] Zhang K, Zuo W, Chen Y, *et al*. Beyond a gaussian denoiser: Residual learning of deep CNN for image denoising [J]. *IEEE Transactions on Image Processing*. 2017, **26**(7):3142-3155.
[27] Xu J, Huang Y, Cheng M M, Liu L, Zhu F, Xu Z, Shao L. Noisy-as-clean: Learning self-supervised denoising from corrupted image [J]. *IEEE Transactions on Image Processing*. 2020, **29**:9316-9329.
[28] El Helou M, Süsstrunk S. Blind universal Bayesian image denoising with Gaussian noise level learning [9]. *IEEE Transactions on Image Processing*. 2020, 29:4885-4897.
[29] Liu D, Wen B, Jiao J, *et al*. Connecting Image Denoising and High-Level Vision Tasks via Deep Learning [J]. *IEEE Transactions on Image Processing*. 2020, **29**:3695-3706.
[30] Tian C, Xu Y, Zuo W. Image denoising using deep CNN with batch renormalization [J]. *Neural Networks*. 2020, **121**:461-473.
[31] Zhang W, Jin L, Song E, *et al*. Removal of impulse noise in color images based on convolutional neural network [J]. *Applied Soft Computing*. 2019, **82**:105558.
[32] Khaw H Y, Soon F C, Chuah J H, *et al*. High-density impulse noise detection and removal using deep convolutional neural network with particle swarm optimization [J]. *IET Image Processing*. 2019, **13**(2):365-374.
[33] Jin L, Zhang W, Ma G, *et al*. Learning deep CNNs for impulse noise removal in images [J]. *Journal of Visual Communication and Image Representation*. 2019, **62**:193-205.
[34] Radlak K, Malinski L, Smolka B. Deep learning-based switching filter for impulsive noise removal in color images [J]. *Sensors*. 2020, **20**(10):2782.
[35] Zhang W, Aljasem K, Zappe H, *et al*. Highly flexible MTF measurement system for tunable micro lenses [J]. *Optics Express*. 2010, **18**(12):12458-112469.
[36] Cabib D, Rahav A, Barak T. Broad-band optical test bench (OPTISHOP) to measure MTF and transmittance of visible and IR optical components [J]. *Infrared Imaging Systems: Design, Analysis, Modeling, and Testing XVIII*. 2007, **6543**: 365-372. SPIE.
[37] Jia J, Wang Y, Cheng X, *et al*. Destriping algorithms based on statistics and spatial filtering for visible-to-thermal infrared pushbroom hyperspectral imagery. *IEEE Transactions on Geoscience and Remote Sensing*. 2019 Feb 3;**57**(6):4077-4091.
[38] Abiko R, Ikehara M. Blind denoising of mixed Gaussian-impulse noise by single CNN [C]. ICASSP 2019-2019 IEEE International Conference on Acoustics, Speech and Signal Processing (ICASSP). 2019, 1717-1721. IEEE.
[39] Adam T, Paramesran R, Mingming Y, *et al*. Combined higher order non-convex total variation with overlapping group sparsity for impulse noise removal [J]. *Multimedia Tools and Applications*. 2021, **80**:18503-18530.
[40] Yin M, Adam T, Paramesran R, *et al*. An ℓ_0-overlapping group sparse total variation for impulse noise image restoration [J]. *Signal Processing: Image Communication*. 2022, **102**:116620.
[41] Li G, Zhang F, Liu Q. Distribution-Transformed Network for Impulse Noise Removal [J]. *Journal of Shanghai Jiaotong University (Science)*. 2021, **26**:543-553.
[42] Wang Z, Bovik A C, Sheikh H R, *et al*. Image quality assessment: from error visibility to structural similarity [J]. *IEEE Transactions on Image Processing*. 2004, **13**(4):600-612.